

Fast dynamics and emergent topological defects in long-range interacting particle systems

Zhenwei Yao*

*School of Physics and Astronomy, and Institute of Natural Sciences,
Shanghai Jiao Tong University, Shanghai 200240, China*

Long-range interacting systems exhibit unusual physical properties not shared by systems with short-range interactions. Understanding the dynamical and statistical effects of long-range interactions yields insights into a host of physical systems in nature and industry. In this work, we investigate the classical microscopic dynamics of screened Coulomb interacting particles confined in the disk, and reveal the featured dynamics and emergent statistical regularities created by the long-range interaction. We highlight the long-range interaction driven fast single-particle and collective dynamics, and the emergent topological defect structure. This work suggests the rich physics arising from the interplay of long-range interaction, topology and dynamics.

I. INTRODUCTION

The classical mechanical model of interacting particles is of great historical and scientific significance [1–3]. Based on the short-range interacting particle model, Ludwig Boltzmann completed the statistical interpretation of thermodynamics, and derived the famous H -theorem that has inspired profound discussions on the foundation of statistical mechanics [2, 4, 5]. Generalizing the physical interaction to the long-range regime invalidates the basic concepts of additivity and extensivity, which constitute the foundation of thermodynamics [6–8]. Long-range interactions are also widely seen in a variety of interdisciplinary systems at length scales covering multiple orders of magnitude [9–13]. Especially, the long-range nature of the electrostatic interaction is crucial for the self-assembly of exceedingly rich soft matters in electrolyte solutions [14–18]. To deal with the notoriously challenging long-range interacting many-body systems, the approach based on numerical integration of the equations of motion at high precision has proven to be a powerful tool to reveal the fundamental microscopic dynamics not accessible by mean-field theories [6, 19]. Elucidating the dynamical effects of long-range interactions yields insights into various nonequilibrium processes ranging from hydrodynamics [9, 10, 12] to electrostatic self-assembly [16, 20–22].

The goal of this work is to investigate the classical dynamics of screened Coulomb interacting particles confined in the disk. This work represents a generalization of the previous studies on the equilibrium packing of charged point particles in the disk from the static to the dynamical regime [23–25]. This theoretical model can be realized by colloidal experiments, where the screening length is tunable by the salt concentration [14, 25–27]. Previous studies of the static disk model show that the inhomogeneity in density created by the long-range repulsion could induce Gaussian curvature and excite topo-

logical defects [23–25, 28]. As a fundamental topological defect, a disclination in a triangular lattice refers to a vertex whose coordination number z deviates from six. The disk model provides the opportunity to clarify a host of questions with broad implications, such as: What is the distinction of short- and long-range interactions in commanding single-particle and collective dynamics? Will the defect structure revealed in the static system still persist in the dynamical regime, and if yes, in which form?

To address these fundamental questions, we resort to the adaptive Verlet method to construct long-time, energy-conserved particle trajectories [19], and reveal the featured energy transfer mode and fast single-particle and collective dynamics under the long-range interaction. By analyzing the convoluted collective dynamics from the unique perspective of topological defects, we identify the emergent statistical regularity in the distribution of topological charges, and uncover the fundamentally different defect structures in short- and long-range interacting systems. The discovery of the emergent dynamical and statistical regularities in this work may have implications in characterizing the intriguing physical effects of long-range interactions.

II. MODEL AND METHOD

The model consists of a collection of N identical point particles of mass m_0 confined in a disk of radius r_0 interacting by the screened Coulomb potential. The Hamiltonian of the system is

$$H = \sum_{i=1}^N \left(\frac{\vec{p}_i^2}{2m} + V_{\text{wall}}(|\vec{x}_i|) \right) + \sum_{i \neq j} V(|\vec{x}_i - \vec{x}_j|). \quad (1)$$

The confining potential

$$V_{\text{wall}}(|\vec{x}_i|) = \frac{1}{2} k_0 (|\vec{x}_i| - r_0)^2 \chi(|\vec{x}_i| - r_0), \quad (2)$$

where $\chi(x) = 1$ if $x > 0$, and $\chi(x) = 0$ otherwise. The screened Coulomb potential

$$V(r) = V_0 \frac{1}{r} e^{-\frac{r}{\lambda}}. \quad (3)$$

*Electronic address: zyao@sjtu.edu.cn

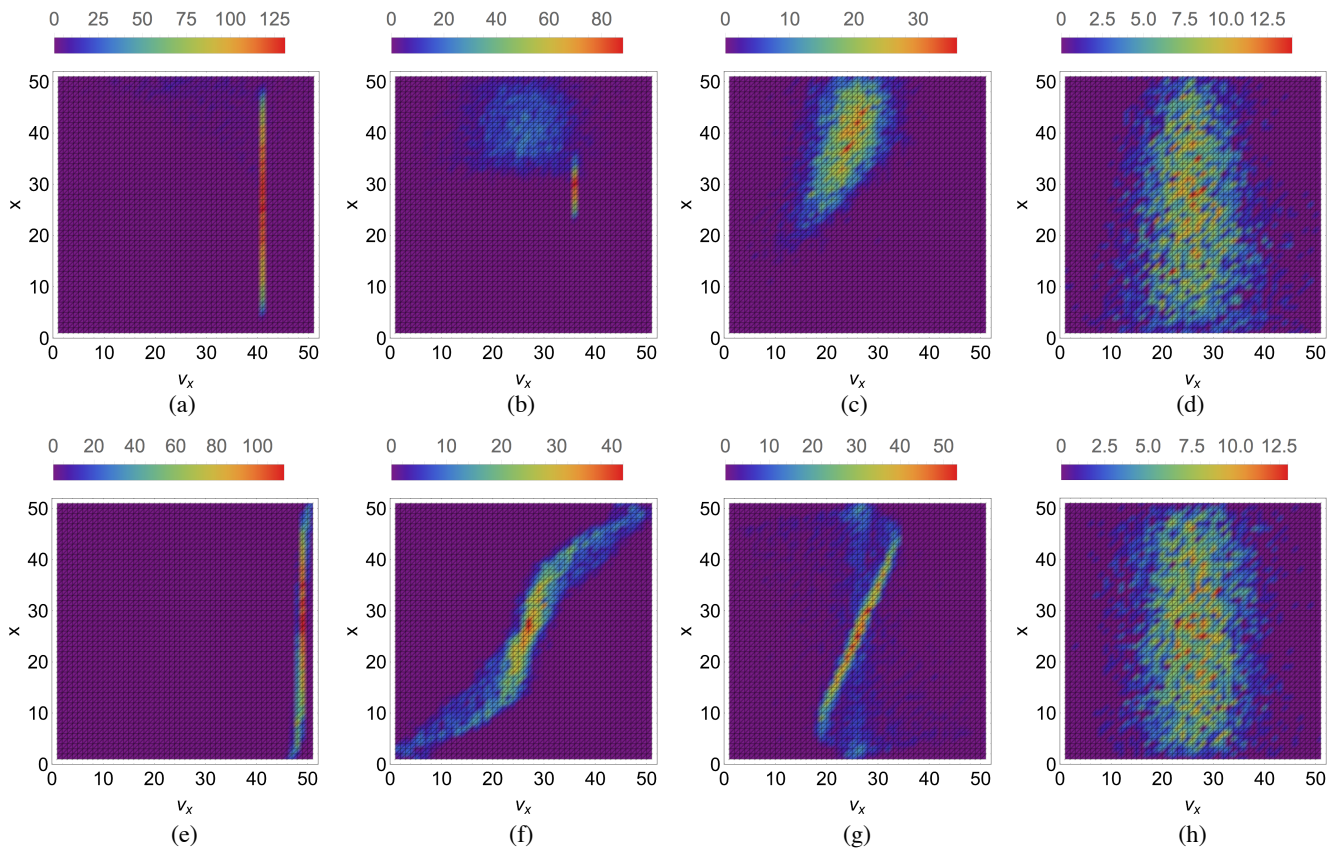


FIG. 1: Short- and long-range interacting particle systems exhibit distinct scenarios of dynamical evolution as represented in the space of $\{x, v_x\}$. (a)-(d) $\lambda/a = 0.05$. $t/\tau_0 = \{0.15, 0.90, 1.35, 5.85\}$. (e)-(h) $\lambda/a = 10$. $t/\tau_0 = \{0.0015, 0.009, 0.036, 6.0\}$. The space is divided into 50×50 cells. The colored legends indicate the number of particles in $\delta x \delta v_x$. $x \in [-x_m, x_m]$ and $v_x \in [-v_m, v_m]$. (a)-(d) $x_m = \{1.0, 1.0, 1.0, 1.0\}$. $v_m = \{1.73, 2.5, 2.7, 3.6\}$. (e)-(h) $x_m = \{1.0, 1.12, 1.13, 1.15\}$. $v_m = \{1.12, 27.1, 44.7, 58.2\}$. $k_0 = 10^5$. $N = 5000$. $V_0 = 1$.

The screened Coulomb potential allows us to investigate the effects of the long-range interaction by comparison with that of the short-range interaction. Note that the charge neutrality condition requires the existence of opposite charges, which are treated as continuum background charges in our model. The model system of charged particles with the effective interaction in the form of Eq.(3) could be experimentally realized by charged polymethyl methacrylate (PMMA) particles in electrolyte solutions [25, 29]. No cut-off length is introduced in the calculation of the long-range interaction force. We distinguish the short- and long-range interactions by the ratio λ/a by physical consideration, where a is the mean distance between nearest particles. Under the assumption that the particles are arranged by triangular lattice, it is estimated that $a/r_0 = \sqrt{2\pi/\sqrt{3}N}$.

The dynamical evolution of the system is governed by the Hamiltonian in Eq.(1). We construct long-time, energy-conserved particle trajectories by the adaptive Verlet method, where the time step is dynamically varying for striking a balance of the energy conservation and the computational efficiency. To highlight the effect of

the interaction range on the relaxation process, the particles are specified with a uniform velocity $\vec{v}(t=0) = v_0 \hat{x}$ in the initial state. The initial positions of the particles are randomly distributed by the standard procedure of random disk packing [30]. We analyze the relaxation process from both perspectives of the H -function and the speed distribution function. In this work, the units of length, mass, time, and energy are r_0 , m_0 , τ_0 , and ϵ_0 , respectively. $\epsilon_0 = m_0(r_0/\tau_0)^2$. $\tau_0 = r_0/v_0$. Typically, $h = 10^{-7}$ and $k_0 = 10^5$ to ensure that the total energy is well conserved and the particles are geometrically confined in the disk in our simulations. More simulation details are presented in Appendix A. The effects of the stiffness k_0 of the confining potential on both the relaxation rate and the particle density distribution are discussed in Appendices B and C.

III. RESULTS AND DISCUSSION

In Fig. 1, we show typical instantaneous states in the dynamical evolution of the system in the space spanned by the parameters x and v_x for $\lambda/a = 0.05$ [Figs. 1(a)-(d)]

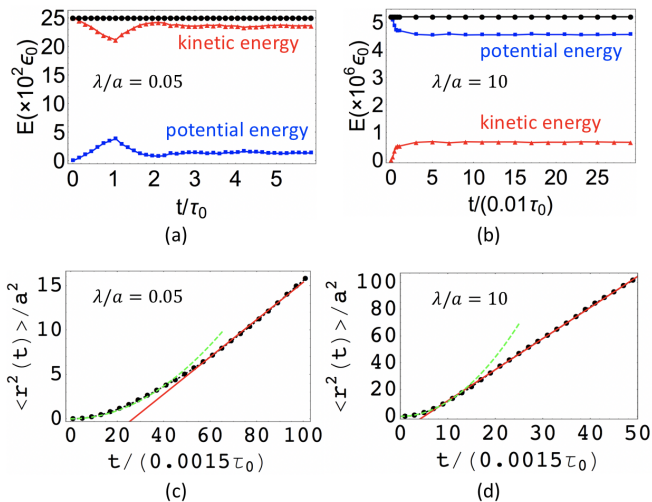


FIG. 2: Fast dynamics under the long-range interaction as demonstrated in the energy transfer process and the single-particle motion. (a) and (b) Temporal variation of the system energy for typical short- and long-range interacting systems. (c) and (d) Plots of the mean squared displacement of a single particle near the center of the disk. The quadratic (dashed green) and linear (solid red) fitting curves indicate the ballistic and diffusive motions. $N = 5000$. $k_0 = 10^5$. $V_0 = 1$.

and $\lambda/a = 10$ [Figs. 1(e)-(h)]. The dynamical evolutions in the complementary space of $\{y, v_y\}$ are presented in Appendix B. $\{x, y, v_x, v_y\}$ constitute a complete single-particle phase space (μ -space), where each point represents one particle with specific position and velocity. The density of the points in the μ -space is indicated by color. We see that the short- and long-range interacting systems exhibit distinct dynamical behaviors. The system of $\lambda/a = 10$ reaches the equilibrium state much faster than that of $\lambda/a = 0.05$. We also notice that, for the case of $\lambda/a = 0.05$, the initial uniform motion of the particles along x-axis leads to the shrinking of the occupied belt-like region, as shown in Fig. 1(b). In contrast, the disk is always fully occupied for the case of $\lambda/a = 10$.

The total mechanical energy of the system is well conserved in the dynamical evolution of the system, as shown in Figs. 2(a) and 2(b). We see that the short- and long-range interacting systems exhibit distinct energy transfer mode between the kinetic and potential energies. Figure 2(b) shows the simultaneous reduction of the potential energy and the increase of the kinetic energy, indicating the conversion of the potential energy to the kinetic energy. In contrast, we find that the situation is opposite for the case of $\lambda/a = 0.05$ in Fig. 2(a). This featured energy transfer scenario is uniformly observed by changing the value of V_0 in the screened Coulomb potential from $V_0 = 0.1$ to $V_0 = 5$ (see Fig. 7 in Appendix B). This observation implies that, for long- and short-range interacting systems with identical initial state, the former system may possess a higher temperature in the final equilibrium state, which will be discussed later. More

information about the dependence of the potential and kinetic energies on λ is presented in Appendix A. Figures 2(a) and 2(b) also show that the kinetic and potential energy curves ultimately become flat, which can be attributed to concurrent inverse collision processes in the many-particle system.

The fast relaxation of the long-range interacting system, as observed in Fig. 1, is also reflected in the variation of the energy curves in Figs. 2(a) and 2(b); note the different time scales in the abscissa axes. A question naturally arises: Do individual particles move faster under the long-range interaction? To address this question, we analyze the dynamics of a randomly picked single particle near the center of the disk to avoid any boundary effect. By averaging over 100 statistically independent particle trajectories, we plot the mean squared displacement $\langle r^2(t) \rangle$ in Figs. 2(c) and 2(d) for both cases of $\lambda/a = 0.05$ and $\lambda/a = 10$. We uniformly observe the shift of the initial ballistic motion (the dashed green quadratic fitting curves) to the diffusive motion (the solid red linear fitting lines). Remarkably, the diffusion coefficient for $\lambda/a = 10$ is about 11 times of that for $\lambda/a = 0.05$. The speed of the initial ballistic motion for the former system is about 48 times faster than the latter one. To conclude, the single particle dynamics is significantly faster under the long-range interaction.

We proceed to discuss the influence of the range of interaction on the collective dynamics. Specifically, we focus on the relaxation of the particle speed in the short- and long-range interacting systems. According to classical statistical physics, if the interaction potential is a function of particle coordinates only, the distribution of the particle speed uniformly conforms to the Maxwell-Boltzmann distribution regardless of the range of interaction [3]. However, the range of interaction may affect the kinetic pathway of the relaxation process. To clarify this question, we quantitatively characterize the relaxation process by both the H function and the quantity δf^2 . As a measure of the deviation of the instantaneous speed distribution $f(v)$ from the Maxwell-Boltzmann distribution f_{eq} , δf^2 is defined as

$$\delta f^2 = \int_0^\infty (f(v) - f_{\text{eq}}(v))^2 dv. \quad (4)$$

The H function measures the relative probability of an out-of-equilibrium state, and its discrete expression is [2]:

$$H = \sum_i n_i \log n_i, \quad (5)$$

where n_i is the number of particles in the i -th cell of the μ -space spanned by $\{x, y, v_x, v_y\}$.

Figures 3(a) and 3(b) show the H - and δf^2 -curves for the cases of $\lambda/a = 0.05$ and $\lambda/a = 10$, respectively. From the H -curves, we see that both systems tend to evolve along the direction of reducing H [3]. The H -curves are subject to persistent fluctuations in equilibrium. One could read the relaxation time from both the H - and

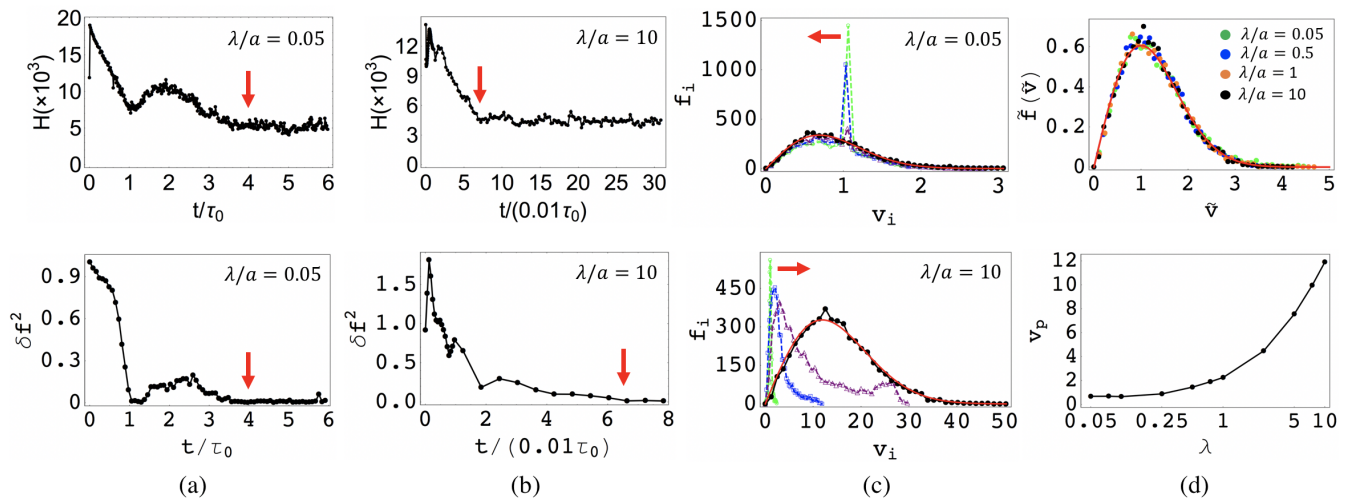


FIG. 3: Fast relaxation of the particle speed under the long-range interaction. (a) $\lambda/a = 0.05$. (b) $\lambda/a = 10$. The relaxation process is characterized by both the H function and the speed distribution function. δf^2 is the deviation of the speed distribution function $f(v)$ from the Maxwell-Boltzmann distribution (see the main text for more information). The red arrows in (a) and (b) indicate the common relaxation time as read from both the H - and δf^2 -curves. (c) Typical instantaneous distribution curves in the relaxation process towards the equilibrium distribution (solid red curves). Upper panel: $t/\tau_0 = 0.77$ (green), 0.86 (blue), 1.0 (purple), and 5.85 (black). Lower panel: $t/\tau_0 = 0.00012$ (green), 0.001 (blue), 0.004 (purple), 6.0 (black). The red arrows indicate the opposite movement of the peak. (d) Uniform collapse of the reduced speed distributions at varying λ on the standard normalized Maxwell-Boltzmann distribution. The plot of the most probable speed v_p against λ is presented in the lower panel. $N = 5000$. $k_0 = 10^5$. $V_0 = 1$.

δf^2 -curves. These curves become stable after the characteristic sites as indicated by the red arrows in Figs. 3(a) and 3(b). And these sites give the value for the relaxation time. The relaxation times as read from both the H - and δf^2 -curves are identical, which implies the consistency of both quantities of H and δf^2 to characterize the relaxation process. Furthermore, comparison of Figs. 3(a) and 3(b) shows the significantly faster relaxation rate under the long-range interaction by two orders of magnitude. We also observe much faster relaxation of the orientation of particle velocity in larger- λ systems (see Appendix B for more information).

Typical instantaneous speed distributions are presented in Fig. 3(c). We see that the short- and long-range interacting systems exhibit distinct kinetic pathways in the relaxation process. The peak in the distribution profile moves along opposite directions in these two kinds of systems as indicated by the arrows. This phenomenon can be understood from Fig. 2. Figure 2(b) shows that the potential energy is converted into kinetic energy for the case of $\lambda/a = 10$. The increase of the kinetic energy leads to the rightward movement of the peak in the lower panel for $\lambda/a = 10$ in Fig. 3(c). This process is reversed for the case of $\lambda/a = 0.05$. Furthermore, in the relaxation of the long-range interacting system, we notice the appearance of a new peak in the tail of the distribution profile [see the purple curve in the lower panel in Fig. 3(c)]. This peak originates from the accumulation of particle population in the high speed regime; the associated extra kinetic energy is provided by the release of the stored potential energy in the long-range repulsive

system [see Fig. 2(b)].

The resulting equilibrium speed distributions indicated by the solid red curves in Fig. 3(c) can be well fitted by the two-dimensional Maxwell-Boltzmann distribution:

$$f(v)\delta v = N \frac{v}{v_p^2} \exp\left(-\frac{v^2}{2v_p^2}\right) \delta v, \quad (6)$$

where the most probable speed $v_p = \sqrt{k_B T/m}$. By rescaling the speed by v_p , all the reduced speed distributions at varying λ uniformly collapse on the standard normalized Maxwell-Boltzmann distribution, as shown in Fig. 3(d). The dependence of v_p on λ is shown in the lower panel in Fig. 3(d). Since $T \propto v_p^2$, we conclude that under the same initial condition the temperature of a larger- λ system in equilibrium is indeed significantly higher.

Now, we analyze the collective dynamics from the perspective of the underlying topological defect structure. For a two-dimensional particle array, one can resort to the standard Delaunay triangulation procedure to identify the particles whose coordination number z is deviated from six [28]. These particles are known as disclinations, carrying topological charge $q = 6 - z$. Elasticity theory shows a remarkable analogy of disclinations and electric charges; oppositely charged disclinations attract and like-signs repel. The concept of topological charge has proven crucial for understanding 2D crystal melting [31, 32], healing of crystalline order [33, 34], packing of twisted filament bundles and virus [35–37], and non-equilibrium dynamics [38, 39].

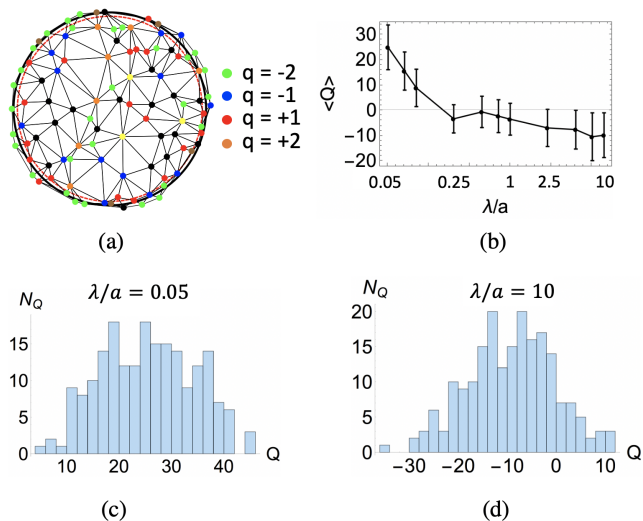


FIG. 4: Short- and Long-range interacting systems exhibit fundamentally different topological defect structures. (a) Classification of the particles by the topological charge. (b) Plot of $\langle Q \rangle$ vs λ . $\langle Q \rangle$ is the mean total topological charge within the circular region indicated by the dashed red circle in (a). Notice that $\langle Q \rangle$ becomes negative at large λ . (c) and (d) show the distributions of Q in statistically independent equilibrium particle configurations for $\lambda/a = 0.05$ and $\lambda/a = 10$, respectively. $N = 5000$. $k_0 = 10^5$. $V_0 = 1$.

In Fig. 4(a), we demonstrate the Delaunay triangulation of an instantaneous particle configuration. Different types of disclinations are indicated with different colors. We focus on the total topological charge Q within the circular region of radius $r = r_0 - a$. Previous studies on the static packing of long-range repulsive particles confined in the disk reveal the negative value for Q , indicating the emergent hyperbolic geometry in the inhomogeneity created by the long-range interaction [23–25]. Here, we generalize the disk model from the static to the dynamical regime, and explore the defect structure in the dynamical long-range interacting system.

We analyze hundreds of statistically independent equilibrium particle configurations at varying λ , and obtain the histograms of the total topological charge Q for the cases of $\lambda/a = 0.05$ and $\lambda/a = 10$ as shown in Figs. 4(c) and 4(d). From Fig. 4(d) for $\lambda/a = 10$, we see that in most equilibrium states the total topological charge is negative. However, equilibrium states with positive Q also exist. In contrast, the value for Q is negative in the static ground state of long-range interacting disk system [23–25]. As such, the dynamical disk model supports richer defect structures. Figure 4(d) shows that the mean value for Q is negative for $\lambda/a = 10$. In contrast, for the case of $\lambda/a = 0.05$ in Fig. 4(c), the total topological charge is uniformly positive in all of the equilibrium states. The dependence of $\langle Q \rangle$ on λ is plotted in Fig. 4(b); we obtain the values for $\langle Q \rangle$ and the error bars by analyzing over 200 statistically independent particle configurations in equilibrium. Figure 4(b) shows

that the value for $\langle Q \rangle$ turns negative with the increase of λ . Therefore, it is in the sense of statistical averaging that the dynamical long-range interacting system preserves the negative $\langle Q \rangle$ -value and the hyperbolic geometry as in the static system.

Finally, we briefly discuss the issue of boundary effect. The confining geometry of the disk brings in the length scale r_0 (the radius of the disk). The degree of the boundary effect may be measured by the ratio λ/r_0 . Calculations show that the value of λ/r_0 is as small as 0.02 for $\lambda/a = 0.75$, when $\langle Q \rangle$ becomes negative as shown in Fig. 4(b). As such, the phenomenon of negative $\langle Q \rangle$ -value reflects the intrinsic dynamical and statistical property of the long-range interacting system. We also notice that the value of λ/r_0 increases from 0.02 ($\lambda/a = 0.75$) to 0.27 ($\lambda/a = 10$). To reduce the boundary effect and meanwhile to retain the effect of long-range interaction, one shall work in the regime of small λ/r_0 and large λ/a . This condition can be fulfilled by specifying a large value for N , since $\lambda/r_0 = (\lambda/a) \times (\sqrt{2\pi/\sqrt{3N}})$. By striking a balance of simulation time and system size, the maximum value for N is 5000 in this work. Since the computation time is a quadratic function of N for simulating long-range interacting systems, it is desirable to employ efficient algorithm to approach the large- N limit for exploring the interested regime of small λ/r_0 and large λ/a . This is beyond the scope of this work.

IV. CONCLUSION

In summary, based on the screened Coulomb interacting disk model, we investigate the dynamical and statistical effects of the long-range interaction by analyzing the classical microscopic dynamics. Specifically, we reveal the fundamental difference of the short- and long-range interactions in the aspects of energy transfer mode, single-particle and collective dynamics, and the underlying defect structure. This work demonstrates the emergent dynamical and statistical regularities in long-range interacting many-particle systems, and suggests the rich physics arising from the interplay of long-range interaction, topology and dynamics.

Acknowledgments

This work was supported by the National Natural Science Foundation of China (Grants No. BC4190050). The author thanks the support from the Student Innovation Center at Shanghai Jiao Tong University.

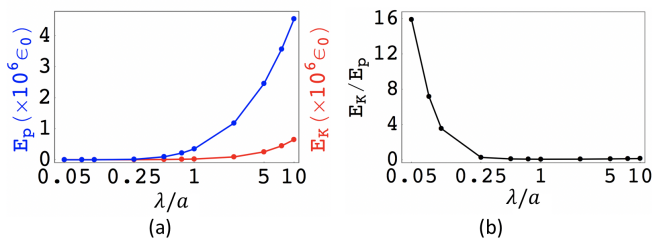


FIG. 5: Plot of the potential energy E_p and the kinetic energy E_k versus λ in equilibrium state. $N = 5000$. $k_0 = 10^5$. $V_0 = 1$.

Appendix A: Simulation details

We employ the adaptive Verlet method to construct long-time particle trajectories [19]. The time step dt is dynamically varying for striking a balance of the energy conservation and computational efficiency.

We denote the trajectory of any particle labelled i as $\{\vec{x}_i(t_j)\}$. From the initial state specified by $\vec{x}_i(t_0)$ and $\dot{\vec{x}}_i(t_0)$, we obtain $\vec{x}_i(t_i = t_0 + h)$ by

$$\vec{x}_i(t+h) = \vec{x}_i(t) + \dot{\vec{x}}_i(t)h + \frac{1}{2}\ddot{\vec{x}}_i(t)h^2 + \mathcal{O}(h^3).$$

$\ddot{\vec{x}}_i(t) = \vec{F}_i(t)/m_0$, $\vec{F}_i(t)$ is the force on the particle i at time t , and m_0 is the mass of the particle. $\vec{F}_i = \sum_{i \neq j} \vec{F}_{ij} + \vec{F}_i^W$, where the first term is the interaction force from all the other particles, and the second term arises if $|\vec{x}_i| > r_0$. According to the adaptive Verlet method, from $\vec{x}_i(t_j)$ and $\vec{x}_i(t_{j-1})$, we have

$$\begin{aligned} \vec{x}_i(t_{j+1}) = \vec{x}_i(t_j) + (\vec{x}_i(t_j) - \vec{x}_i(t_{j-1})) \frac{dt_j}{dt_{j-1}} \\ + \ddot{\vec{x}}_i(t_j) \frac{dt_j + dt_{j-1}}{2} dt_j. \end{aligned} \quad (7)$$

For uniform time step $dt_j = h$, the above equation reduces to the ordinary Verlet integration scheme:

$$\vec{x}_i(t+2h) = 2\vec{x}_i(t+h) - \vec{x}_i(t) + \ddot{\vec{x}}_i(t+h)h^2 + \mathcal{O}(h^4).$$

We employ the procedure of random disk packing to generate the initial random configuration [30]. Specifically, the disks of radius r_d are placed within the circle of radius r_0 in sequence. In this process, each newly added disk shall not overlap any existent disk. The centers of the disks constitute the initial positions of the point particles. Typically, the value of r_d is about $0.3a$, where a is the mean distance of nearest particles. The reason of using random disk packing instead of random point packing is as follows. Simulations show that random point packing could lead to aggregation of particles. The resulting large force requires a very fine time step to fulfill the conservation law of energy, which significantly slows down the dynamical evolution of the system in simulations.

The total mechanical energy in our simulations is well conserved at a high precision up to several decimal digits

in the energy value. In the main text, we have shown the temporal variation of the kinetic and potential energies. Here, in Fig. 5, we plot the kinetic and potential energies versus λ in equilibrium state. From Fig. 5(a), we see that the potential energy increases much faster than the kinetic energy. Furthermore, Fig. 5(b) shows the rapid decline of the ratio E_k/E_p with the increase of λ .

Appendix B: More information about relaxation kinetics

Typical instantaneous states in the dynamical evolution of the system in the space spanned by x and v_x are presented in Fig. 1 in the main text. In Fig. 6, we further present the identical dynamical evolutions as in Fig. 1 in the complementary space of $\{y, v_y\}$. It is observed that for the case of $\lambda/a = 10$, the patterns in both spaces of $\{x, v_x\}$ and $\{y, v_y\}$ become similar after $t/\tau_0 = 0.009$ [see Fig. 1(f) and Fig. 6(f)]. In other words, the distribution function for the system of $\lambda/a = 10$ becomes symmetric with respect to (x, v_x) and (y, v_y) in a much faster fashion in comparison with the system of $\lambda/a = 0.05$.

In Fig. 7, we show the temporal variation of the kinetic and potential energies for typical short- and long-range interacting systems under varying V_0 . The value of V_0 reflects the strength of the screened Coulomb potential, as shown in Eq.(3). Since V_0 is measured in the unit of $m_0 r_0 v_0^2$, varying V_0 is equivalent to changing the value of the initial speed v_0 . Figure 7 shows that the conversion of kinetic and potential energies in either short- or long-range interacting systems conforms to a common scenario as the value of V_0 is varied from $V_0 = 0.1$ to $V_0 = 5$. We also notice that unlike the case of $\lambda/a = 10$ [the lower panels in Figs. 7(d)-7(f)], the total energy of the systems with $\lambda/a = 0.05$ is almost invariant as the value of V_0 is varied. This could be attributed to the short-range nature of the interaction, which resembles a hard repulsion at short distance.

In Figs. 8(a) and 8(b), we present typical instantaneous distributions of the orientation of the particle velocity in the relaxation process for $\lambda/a = 0.05$ and $\lambda/a = 10$, respectively. θ is the angle between the direction of the particle velocity and x-axis. Similar to the relaxation of particle speed, the relaxation of θ in the long-range interacting system is also much faster than that in the short-range interacting system.

In Figs. 9(a) and 9(b), we show the temporal variation of the H function under a softer confining potential for $\lambda/a = 0.05$ and $\lambda/a = 10$, respectively. Here, $k_0 = 10^4$, which is ten times less than the case we have discussed in the main text. In comparison with the H -curves in Figs.3(a) and 3(b) in the main text, we find that a softer confining potential tends to significantly slow the relaxation kinetics for the long-range interacting system. The relaxation time increases from about $0.07\tau_0$ at $k_0 = 10^5$ to about $0.2\tau_0$ at $k_0 = 10^4$. In contrast, the relaxation rate of the short-range interacting system is unaffected

by the stiffness of the boundary wall.

Appendix C: Distribution of particle density in equilibrium

Figures 10(a) and 10(b) show the square root of the cumulative particle distribution in equilibrium particle configurations. $n(r)$ is the total number of particles inside the circle of radius r . We find that the $\sqrt{n(r)}$ curve for $\lambda/a = 0.05$ is linear in the interval $r/r_0 \in [0, 1]$ in both Figs. 10(a) and 10(b), where r_0 is the radius of the

disk. The linearity of $\sqrt{n(r)}$ with r indicated a uniform distribution of particles, since $\sqrt{n(r)} = \sqrt{\pi\rho_0}r \propto r$ for a uniform particle distribution of density ρ_0 . Figure 10 shows that changing the stiffness of the confining potential leads to the variation of the particle density for the long-range interacting system. More particles are accumulated near a softer boundary, which reduces the particle density within the disk. In contrast, for the short-range interacting system, the particle density distribution is almost unaffected by the stiffness of the confining potential.

-
- [1] C. Cercignani et al., *Ludwig Boltzmann: The Man Who Trusted Atoms* (Oxford University Press, Oxford, 1998).
- [2] L. Boltzmann, *Lectures On Gas Theory* (University of California Press, Berkeley, 1964).
- [3] S. Ma, *Statistical Mechanics* (World Scientific, Singapore, 1985).
- [4] P. Ehrenfest and T. Ehrenfest, *The Conceptual Foundations of The Statistical Approach in Mechanics* (Courier Corporation, Massachusetts, 2002).
- [5] D. Frenkel and S. Louët, *Eur. Phys. J. E* **39**, 68 (2016).
- [6] A. Campa, T. Dauxois, D. Fanelli, and S. Ruffo, *Physics of Long-Range Interacting Systems* (Oxford University Press, Oxford, UK, 2014).
- [7] Y. Levin, R. Pakter, F. B. Rizzato, T. N. Teles, and F. P. Benetti, *Phys. Rep.* **535**, 1 (2014).
- [8] R. Pakter and Y. Levin, *J. Stat. Mech: Theory Exp.* **2017**, 044001 (2017).
- [9] J. Lighthill, *SIAM Rev* **18**, 161 (1976).
- [10] S. Chattopadhyay and X.-L. Wu, *Biophys. J.* **96**, 2023 (2009).
- [11] C. Tabi, A. Mohamadou, and T. Kofané, *Eur. Phys. J. E* **32**, 327 (2010).
- [12] M. C. Dallaston, M. A. Fontelos, D. Tseluiko, and S. Kalliadasis, *Phys. Rev. Lett.* **120**, 034505 (2018).
- [13] Z. Yao, *Phys. Rev. Lett.* **122**, 228002 (2019).
- [14] C. Holm, P. Kélicheff, and R. Podgornik, *Electrostatic Effects in Soft Matter and Biophysics* (Springer, Berlin, 2001).
- [15] Y. Levin, *Rep. Prog. Phys.* **65**, 1577 (2002).
- [16] D. A. Walker, B. Kowalczyk, M. Olvera de la Cruz, and B. A. Grzybowski, *Nanoscale* **3**, 1316 (2011).
- [17] A. Toor, T. Feng, and T. P. Russell, *Eur. Phys. J. E* **39**, 1 (2016).
- [18] C. Gao, S. Kewalramani, D. M. Valencia, H. Li, J. M. McCourt, M. Olvera de la Cruz, and M. J. Bedzyk, *Proc. Natl. Acad. Sci. U.S.A.* **116**, 22030 (2019).
- [19] D. Rapaport, *The Art of Molecular Dynamics Simulation* (Cambridge University Press, Cambridge, UK, 2004).
- [20] B. A. Grzybowski, A. Winkelman, J. A. Wiles, Y. Brumer, and G. M. Whitesides, *Nat. Mater.* **2**, 241 (2003).
- [21] G. Vernizzi, G. I. Guerrero-García, and M. Olvera de la Cruz, *Phys. Rev. E* **84**, 016707 (2011).
- [22] E. B. Lindgren, I. N. Derbenev, A. Khachatourian, H.-K. Chan, A. J. Stace, and E. Besley, *J. Chem. Theory Comput.* **14**, 905 (2018).
- [23] A. Mughal and M. Moore, *Phys. Rev. E* **76**, 011606 (2007).
- [24] Z. Yao and M. Olvera de la Cruz, *Phys. Rev. Lett.* **111**, 115503 (2013).
- [25] V. Soni, L. R. Gómez, and W. T. Irvine, *Phys. Rev. X* **8**, 011039 (2018).
- [26] P. Debye, *Physikalische Zeitschrift* **24**, 185 (1923).
- [27] A. Dobrynin and M. Rubinstein, *Prog. Polym. Sci.* **30**, 1049 (2005).
- [28] D. R. Nelson, *Defects and Geometry in Condensed Matter Physics* (Cambridge University Press, Cambridge, 2002).
- [29] Y. Chen, Z. Yao, S. Tang, H. Tong, T. Yanagishima, H. Tanaka, and P. Tan, *Nat. Phys.* **17**, 121 (2020).
- [30] B. D. Lubachevsky and F. H. Stillinger, *Journal of Statistical Physics* **60**, 561 (1990).
- [31] J. M. Kosterlitz and D. J. Thouless, *J. Phys. C: Solid State Phys.* **6**, 1181 (1973).
- [32] B. Halperin and D. R. Nelson, *Phys. Rev. Lett.* **41**, 121 (1978).
- [33] W. T. Irvine, M. J. Bowick, and P. M. Chaikin, *Nat. Mater.* **11**, 948 (2012).
- [34] Z. Yao and M. Olvera de la Cruz, *Proc. Natl. Acad. Sci. U.S.A.* **111**, 5094 (2014).
- [35] R. D. Kamien and D. R. Nelson, *Phys. Rev. Lett.* **74**, 2499 (1995).
- [36] G. M. Grason, *Phys. Rev. Lett.* **105**, 045502 (2010).
- [37] J. Lidmar, L. Mirny, and D. R. Nelson, *Phys. Rev. E* **68**, 051910 (2003).
- [38] M. Marchetti, J. Joanny, S. Ramaswamy, T. Liverpool, J. Prost, M. Rao, and R. A. Simha, *Rev. Mod. Phys.* **85**, 1143 (2013).
- [39] F. C. Keber, E. Loiseau, T. Sanchez, S. J. DeCamp, L. Giomi, M. J. Bowick, M. C. Marchetti, Z. Dogic, and A. R. Bausch, *Science* **345**, 1135 (2014).

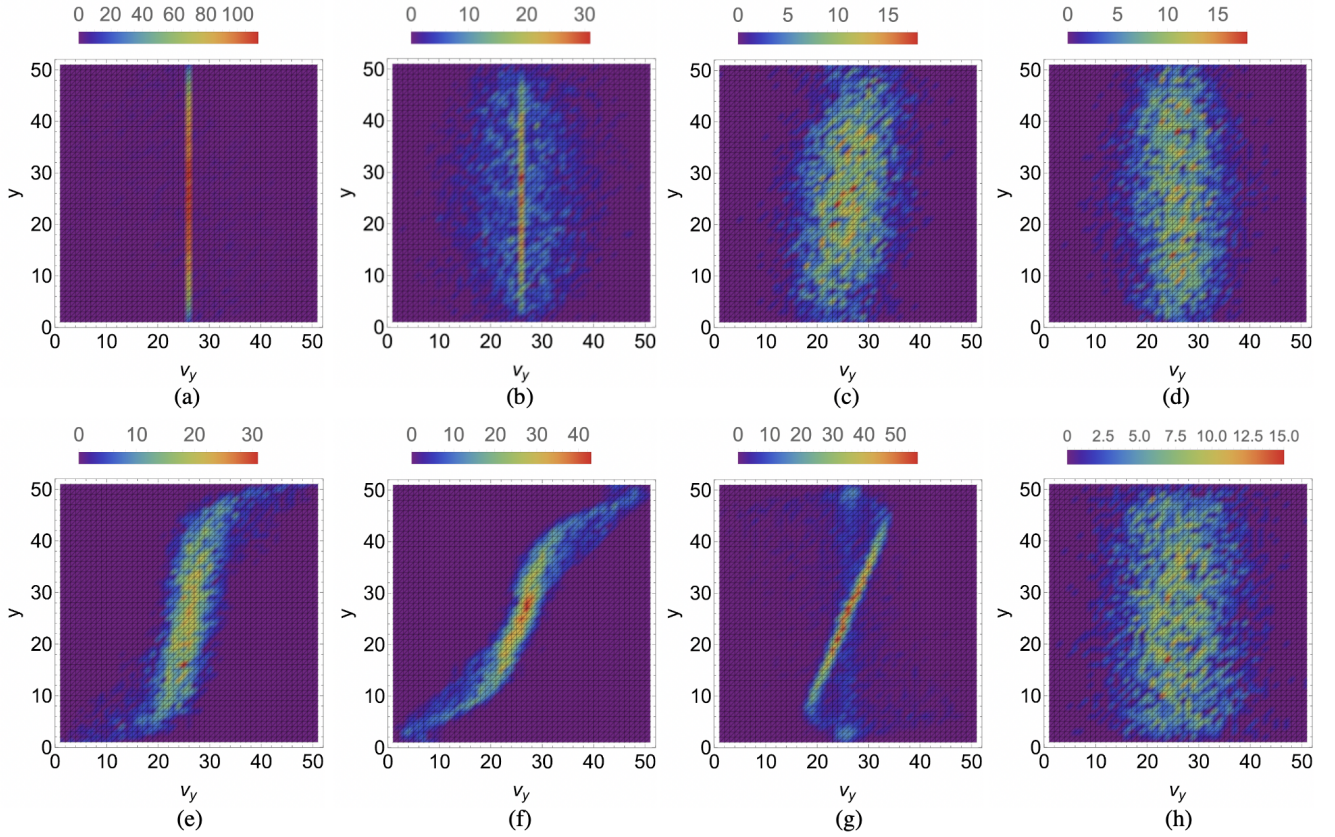


FIG. 6: Short- and long-range interacting particle systems exhibit distinct scenarios of dynamical evolution as represented in the space of $\{y, v_y\}$. (a)-(d) $\lambda/a = 0.05$. $t/\tau_0 = \{0.15, 0.90, 1.35, 5.85\}$. (e)-(h) $\lambda/a = 10$. $t/\tau_0 = \{0.0015, 0.009, 0.036, 6.0\}$. The space is divided into 50×50 cells. The colored legends indicate the number of particles in $\delta y \delta v_y$. $y \in [-y_m, y_m]$ and $v_y \in [-v_m, v_m]$. (a)-(d) $y_m = \{1.0, 0.9, 1.0, 1.0\}$. $v_m = \{1.92, 2.6, 2.83, 3.24\}$. (e)-(h) $y_m = \{1.01, 1.12, 1.12, 1.15\}$. $v_m = \{16.40, 28.50, 42.21, 59.23\}$. $k_0 = 10^5$. $N = 5000$. $V_0 = 1$.

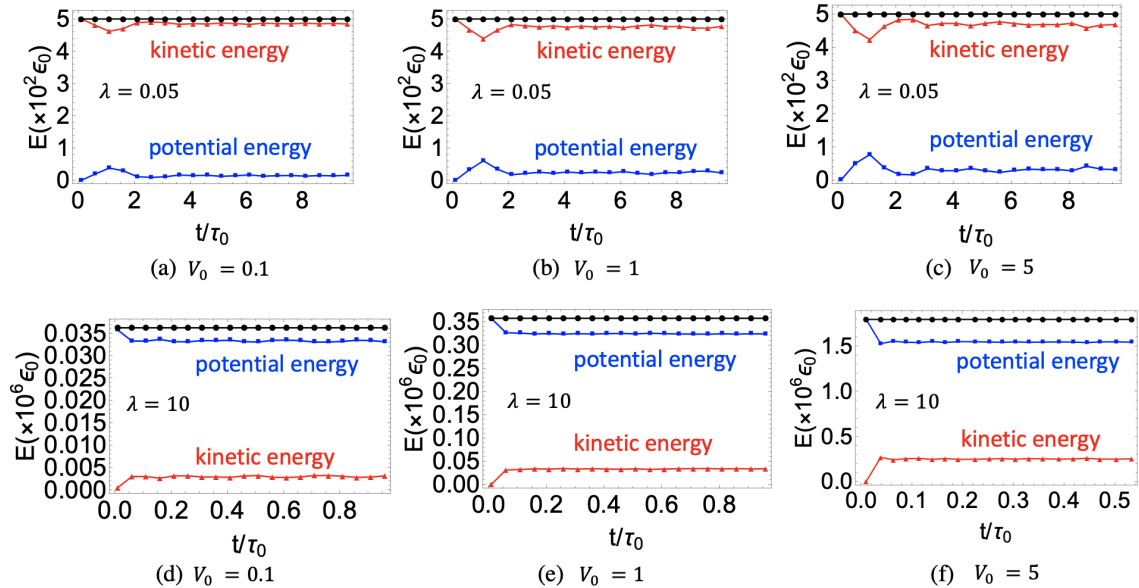


FIG. 7: Temporal variation of the kinetic (red curves) and potential (blue curves) energies for typical short- and long-range interacting systems under varying strength V_0 of the screened Coulomb potential. $N = 1000$. $k_0 = 10^5$.

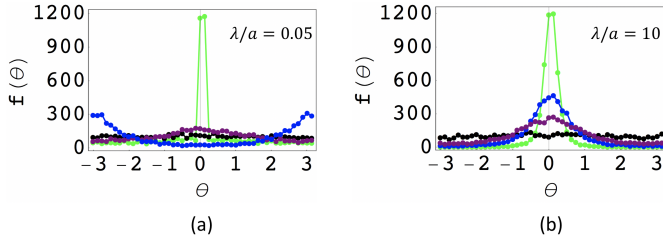


FIG. 8: Relaxation of the orientation of the particle velocity for $\lambda/a = 0.05$ (a) and $\lambda/a = 10$ (b). θ is the angle between the direction of the particle velocity and x-axis. In (a), $t/\tau_0 = 0.57$ (green), 2.07 (blue), 3.57 (purple), and 5.85 (black). In (b), $t/\tau_0 = 0.0001$ (green), 0.0003 (blue), 0.0006 (purple), and 0.01 (black). $N = 5000$. $k_0 = 10^5$. $V_0 = 1$.

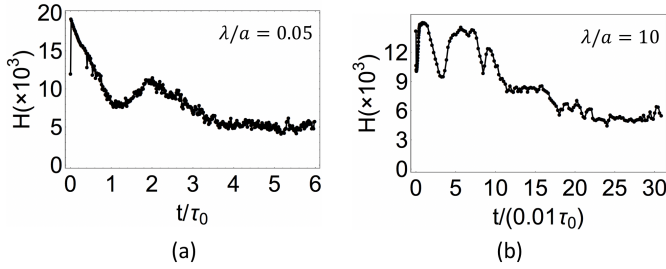


FIG. 9: Temporal variation of the H curve under a softer confining potential in comparison with that in the main text. $k_0 = 10^4$. $\lambda/a = 0.05$ (a) and $\lambda/a = 10$ (b). The H curve for $\lambda/a = 10$ (b) takes longer time to become stable than that at $k_0 = 10^5$. In contrast, the H curve for $\lambda/a = 0.05$ (a) is almost identical to Fig.3a in the main text for $\lambda/a = 0.05$ and $k_0 = 10^5$. $N = 5000$. $V_0 = 1$.

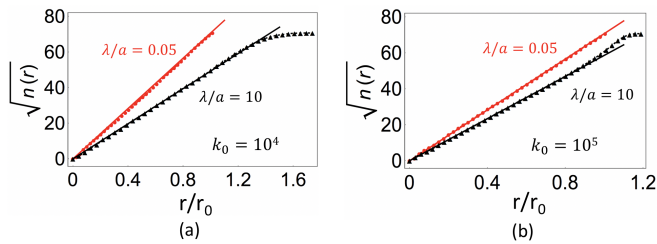


FIG. 10: Plot of the square root of the cumulative particle distribution $\sqrt{n(r)}$ in equilibrium configurations. $k_0 = 10^4$ (a). $k_0 = 10^5$ (b). The solid red lines represent the uniform distribution of particles. $N = 5000$. $V_0 = 1$.